Nonlinear Ekman effects in rotating barotropic flows

By L. ZAVALA SANSÓN AND G. J. F. VAN HEIJST

J. M. Burgers Centre, Department of Physics, Eindhoven University of Technology,
P.O. Box 513, 5600 MB Eindhoven, The Netherlands

In the presence of background rotation, conventional two-dimensional models of geostrophic flow in a rotating system usually include Ekman friction – associated with the no-slip condition at the bottom – by adding a linear term in the vorticity evolution equation. This term is proportional to $E^{1/2}$ (where E is the Ekman number), and arises from the linear Ekman theory, which yields an expression for the vertical velocity produced by the thin Ekman layer at the flat bottom. In this paper, a two-dimensional model with Ekman damping is proposed using again the linear Ekman theory, but now including nonlinear Ekman terms in the vorticity equation. These terms represent nonlinear advection of relative vorticity as well as stretching effects. It is shown that this modified two-dimensional model gives a better description of the spin-down of experimental barotropic vortices than conventional models. Therefore, it is proposed that these corrections should be included in studies of the evolution of quasi-two-dimensional flows, during times comparable to the Ekman period.

1. Introduction

This study revisits the problem of bottom damping effects on barotropic, quasi-two-dimensional flows with background rotation over a flat surface. Examples of such flows are large-scale coherent structures frequently observed in the atmosphere and the ocean as well as in laboratory experiments (in a rotating fluid tank), which are usually only slightly affected by the no-slip boundary condition at the bottom (it is stressed, however, that laboratory experiments are strongly simplified models of large-scale vortices affected by the Earth's rotation). Essentially, the presence of a bottom (topography) induces a three-dimensional effect, which breaks the two-dimensional character of the flow. However, the weakness of bottom damping effects allows their incorporation in a two-dimensional physical model (for this reason the term 'quasi' is used). In particular, this type of dynamics plays an important role in the evolution and decay of barotropic (density-homogeneous) vortices in laboratory experiments (see e.g. van Heijst, Kloosterziel & Williams 1991; Kloosterziel & van Heijst 1992; Orlandi & van Heijst 1992; Maas 1993; henceforth referred to as vH91, KvH92, OvH92 and M93, respectively). In this paper, a physical model describing two-dimensional flows in the presence of weak bottom damping effects is derived in order to study the behaviour of laboratory vortices. The results are compared with the studies cited above and with the predictions of conventional two-dimensional models.

Taking advantage of the predominantly two-dimensional motion in rotating fluid systems with small or moderate Rossby number (i.e. in which the geostrophic balance

dominates), bottom friction can be incorporated in the two-dimensional evolution equation. The crucial step consists of vertical integration of the continuity equation (since the flow is two-dimensional) and use of appropriate expressions for the vertical velocity induced by the Ekman boundary layers at the free-surface and at the bottom. Such velocities can be obtained by using linear theory for the Ekman layers, either at the free surface (due to wind stress, which will not be considered here, however) or at the no-slip bottom. The thickness of the Ekman boundary layer, δ_E, is of order $(\nu/\Omega)^{1/2}$ (with ν the kinematic viscosity and Ω the background rotation rate), which is usually very thin compared with the total fluid depth H. The linear Ekman theory predicts that the vertical velocity on top of the Ekman layer is proportional to the relative vorticity in the interior flow. Although this vertical velocity is much smaller than the horizontal velocities, it does affect the flow evolution. This effect is usually incorporated in the quasi-geostrophic vorticity equation (for a homogeneous flow) by adding a linear term, which measures the stretching effects induced by this Ekman 'suction' (Pedlosky 1987, section 4.6). In numerous papers, Ekman friction has also been included in the two-dimensional vorticity equation using the same result (e.g. by OvH92, among many others). The basic assumption in these models is that the nonlinear terms appearing in the vorticity equation, when the Ekman condition is applied, are negligible. As will be shown in the next section, this assumption can be relaxed and the resulting new, nonlinear Ekman friction terms, although rather small, lead to significant differences compared to the conventional approximation. In particular, they explain the observed decay of barotropic laboratory vortices more satisfactorily than models based on the linear formulation.

Thus, the quasi-two-dimensional model developed here simply retains all the Ekman damping terms (linear and nonlinear). The model can be expressed in an ω–ψ formulation, with the relative vorticity (ω) and stream function (ψ) related through a Poisson equation, as in the purely two-dimensional case. However, the horizontal velocities have a correction of order $O(\delta_E/H) = O(E^{1/2})$ (where E is the Ekman number), which is absent in the conventional two-dimensional model.

An alternative approximation was given by Wedemeyer (1964) for the spin-up problem in an axisymmetric flow. The Wedemeyer model has been reformulated by several authors for the study of the spin-down of barotropic vortices in a rotating fluid tank (see e.g. KvH92, M93) or for the study of the spin-up process in non-axisymmetric containers (van de Konijnenberg 1995). This model allows analytical solutions for axisymmetric flows, under certain restrictions. The obvious limitation of this approximation is the assumption of axisymmetry. Later in this paper it is shown that the Wedemeyer model is a special case of the present approximation.

The rest of the paper is organized as follows. The model is derived in §2. It is possible, although not straightforward, to extend the present theory to the case of a non-flat bottom (work is in progress on the study of Ekman damping over irregular topographies). In §3, the model is tested by numerically solving the vorticity equation and comparing the results with laboratory experiments on the decay of isolated and non-isolated vortices. Also, a comparison is made with the conventional two-dimensional models. Finally, in §4 the results are discussed.

2. Ekman damping over a flat bottom

In this section, a quasi-two-dimensional model is derived, which includes the effects of the Ekman damping associated with a flat bottom. In order to derive a two-dimensional model in a rotating fluid system, the basic assumption is that the
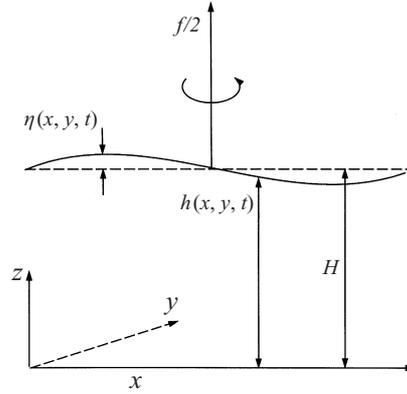
FIGURE 1. Schematic view of a homogeneous fluid layer over a flat bottom in a rotating system.

geostrophic balance dominates the flow evolution. This assumption implies that the horizontal velocities, perpendicular to the axis of rotation, can be considered as depth-independent (Taylor–Proudman theorem). A geostrophic balance is established for small Rossby numbers, i.e. when the relative horizontal accelerations are small compared with Coriolis accelerations and horizontal pressure gradients. In laboratory experiments in a rotating fluid tank, even flows with moderate Rossby number values (e.g. 0.6, see M93) have been observed to show a two-dimensional behaviour, except in the Ekman boundary layer at the bottom. Therefore, the depth-independence of the horizontal motion under typical experimental conditions can be considered as a reasonable approximation for modelling this type of flow.

The depth-independence of the horizontal velocities permits integration of the continuity equation in the vertical direction, from which an expression for the vertical velocity is obtained. Afterwards, the effect of the Ekman layer on the interior flow is incorporated by considering the Ekman condition (the vertical velocity induced by the Ekman layer at the bottom). The Ekman condition is a result of the linear Ekman theory, which assumes geostrophic balance in the interior flow. It has been found in numerous experimental studies, however, that the Ekman condition is a good approximation for introducing the effects of bottom damping even for moderately nonlinear flows (see e.g. M93; KvH92). The results of the present paper also confirm the validity of this approximation.

2.1. *The model*

Using Cartesian coordinates, the horizontal momentum equations and the continuity equation for a homogeneous fluid layer in a rotating system are (see figure 1)

$$\frac{\partial u}{\partial t} + u\frac{\partial u}{\partial x} + v\frac{\partial u}{\partial y} - fv = -\frac{1}{\rho}\frac{\partial P}{\partial x} + \nu\nabla^2 u, \tag{2.1}$$

$$\frac{\partial v}{\partial t} + u\frac{\partial v}{\partial x} + v\frac{\partial v}{\partial y} + fu = -\frac{1}{\rho}\frac{\partial P}{\partial y} + \nu\nabla^2 v, \tag{2.2}$$

$$\frac{\partial u}{\partial x} + \frac{\partial v}{\partial y} + \frac{\partial w}{\partial z} = 0, \tag{2.3}$$

where the z-derivatives have been neglected. Here, (u, v, w) are the velocity components in the (x, y, z) directions, respectively, where z is aligned with the gravitational acceleration $\boldsymbol{g} = (0, 0, -g)$, u and v are assumed z-independent, $f = 2\Omega$ is the Coriolis param-

eter with Ω the rotation rate of the system, t is the time, ν is the kinematic viscosity, $\nabla^2 = \partial^2/\partial x^2 + \partial^2/\partial y^2$ is the horizontal Laplacian operator and ρ is the constant fluid density. The reduced pressure P is

$$P = p + \rho g z - \tfrac{1}{8}\rho f^2 r^2, \tag{2.4}$$

where $p(x, y, z, t)$ is the thermodynamic pressure, and the last term represents the pressure associated with the system's rotation, r being the distance from the rotation axis. In the vertical direction, the motion is confined between

$$0 \leqslant z \leqslant H + \eta \equiv h, \tag{2.5}$$

where H is the layer depth in the absence of any relative motion and $\eta(x, y, t)$ is the free-surface elevation relative to H. Note that η contains the elevation associated with the parabolic shape of the free surface $(f^2 r^2/8g)$ together with the elevation associated with the flow motion, which might be time-dependent. In the vertical direction the hydrostatic balance is assumed to apply. The vertical velocity can be obtained from the horizontal velocities by integrating the continuity equation in the vertical direction.

As usual, the pressure gradients are eliminated by taking the y-derivative of (2.1) and subtracting it from the x-derivative of (2.2), yielding the vorticity equation:

$$\frac{\partial \omega}{\partial t} + u \frac{\partial \omega}{\partial x} + v \frac{\partial \omega}{\partial y} + \left(\frac{\partial u}{\partial x} + \frac{\partial v}{\partial y}\right)(\omega + f) = \nu \nabla^2 \omega, \tag{2.6}$$

where $\omega = \partial v/\partial x - \partial u/\partial y$ is the relative vorticity.

Two-dimensional models are constructed by deriving adequate expressions to substitute the horizontal velocity components (u and v) and the horizontal divergence ($\partial u/\partial x + \partial v/\partial y$) in equation (2.6). These expressions are obtained by integrating the continuity equation over the fluid depth, i.e. from $z = 0$ to $z = h$. Under the assumption that u and v are z-independent in the interior (i.e. outside boundary layers), this integration yields

$$\left(\frac{\partial u}{\partial x} + \frac{\partial v}{\partial y}\right) h = -(w|_{z=h} - w|_{z=0}). \tag{2.7}$$

Ignoring wind stress, the vertical velocity on the free surface is given by the kinematic condition

$$w|_{z=h} = \frac{Dh}{Dt}, \tag{2.8}$$

where D/Dt is the material derivative.

The thin Ekman layer at the bottom generally induces a non-zero vertical velocity. For flat bottom topographies and low Rossby numbers, this velocity is proportional to the relative vorticity of the interior flow outside the Ekman layer; this is expressed by the so-called Ekman condition:

$$w|_{z=0} = \tfrac{1}{2}\delta_E \omega, \tag{2.9}$$

where the thickness of the Ekman layer is

$$\delta_E = \left(\frac{2\nu}{f}\right)^{1/2}. \tag{2.10}$$

With (2.8) and (2.9) the horizontal divergence in (2.7) may be written as

$$\frac{\partial u}{\partial x} + \frac{\partial v}{\partial y} = -\frac{1}{h}\frac{Dh}{Dt} + \frac{1}{2}\frac{\delta_E}{h}\omega. \tag{2.11}$$

This expression states that the horizontal divergence is caused by changes in the fluid depth associated with free-surface variations and by the vertical velocity induced by the Ekman layer at the flat bottom (effects of topography are excluded here). Considering $\eta \ll H$, the free-surface effects can be filtered out from the continuity equation by approximating $h \approx H$ and $Dh/Dt \approx 0$. Equation (2.11) then becomes

$$\frac{\partial u}{\partial x} + \frac{\partial v}{\partial y} = \tfrac{1}{2} E^{1/2} \omega, \tag{2.12}$$

where $E^{1/2} = \delta_E / H$, with $E = 2v/(fH^2)$ the Ekman number.

Substitution of (2.12) in (2.6) yields

$$\frac{\partial \omega}{\partial t} + u\frac{\partial \omega}{\partial x} + v\frac{\partial \omega}{\partial y} = v\nabla^2 \omega - \tfrac{1}{2} E^{1/2} \omega(\omega + f). \tag{2.13}$$

At this point, it is still necessary to obtain suitable expressions for u and v in the nonlinear terms on the left-hand side of this equation. This is achieved by rewriting (2.12) as

$$\frac{\partial}{\partial x}(u - \tfrac{1}{2} E^{1/2} v) + \frac{\partial}{\partial y}(v + \tfrac{1}{2} E^{1/2} u) = 0 \tag{2.14}$$

and by defining a stream function ψ such that

$$u - \tfrac{1}{2} E^{1/2} v = \frac{\partial \psi}{\partial y}, \tag{2.15}$$

$$v + \tfrac{1}{2} E^{1/2} u = -\frac{\partial \psi}{\partial x}. \tag{2.16}$$

From these equations, the corresponding expressions for the velocities in terms of the stream function are obtained:

$$u = \frac{1}{1 + \tfrac{1}{4}E}\left(\frac{\partial \psi}{\partial y} - \tfrac{1}{2} E^{1/2}\frac{\partial \psi}{\partial x}\right), \tag{2.17}$$

$$v = \frac{1}{1 + \tfrac{1}{4}E}\left(-\frac{\partial \psi}{\partial x} - \tfrac{1}{2} E^{1/2}\frac{\partial \psi}{\partial y}\right). \tag{2.18}$$

Retaining $O(1)$ and $O(E^{1/2})$ terms (since $E \ll 1$), the horizontal velocities can be written as

$$u = \frac{\partial \psi}{\partial y} - \tfrac{1}{2} E^{1/2}\frac{\partial \psi}{\partial x}, \tag{2.19}$$

$$v = -\frac{\partial \psi}{\partial x} - \tfrac{1}{2} E^{1/2}\frac{\partial \psi}{\partial y}. \tag{2.20}$$

By inserting (2.19) and (2.20) in the definition of the relative vorticity ($\omega = \partial v/\partial x - \partial u/\partial y$) it is verified that

$$\omega = -\nabla^2 \psi. \tag{2.21}$$

Note that the $O(E^{1/2})$ correction in the horizontal velocities is actually a potential flow, since it vanishes when the curl of the velocity field is taken.

Finally, by substituting (2.19) and (2.20) in (2.13) one arrives at the following evolution equation for the relative vorticity:

$$\frac{\partial \omega}{\partial t} + J(\omega, \psi) - \tfrac{1}{2} E^{1/2}\nabla\psi \cdot \nabla\omega = v\nabla^2\omega - \tfrac{1}{2} E^{1/2}\omega(\omega + f), \tag{2.22}$$

where J is the Jacobian operator. The horizontal velocities (2.19) and (2.20), the Poisson equation (2.21) and the vorticity evolution equation (2.22), represent the ω–ψ formulation of the two-dimensional model, including the flat-bottom Ekman damping (henceforth this is referred to as *model M1*).

2.2. *Comparison with conventional models*

The conventional two-dimensional model including bottom damping, used in many previous studies, only considers the linear part of the Ekman suction in the vorticity equation (*model M2*):

$$\frac{\partial \omega}{\partial t} + J(\omega, \psi) = \nu \nabla^2 \omega - \tfrac{1}{2} E^{1/2} f \omega. \qquad (2.23)$$

Under this approximation, ω and ψ are related through the Poisson equation (2.21), but the horizontal velocities do not include the $O(E^{1/2})$ correction as in (2.19) and (2.20).

The model M1 can be straightforwardly reduced to the purely two-dimensional model (hereafter, *model M3*) by dropping the Ekman terms (which originate from applying the Ekman condition (2.9) at the bottom):

$$\frac{\partial \omega}{\partial t} + J(\omega, \psi) = \nu \nabla^2 \omega. \qquad (2.24)$$

As in model M2, the horizontal velocities do not include the $O(E^{1/2})$ correction, and the relative vorticity and stream function are again related through the Poisson equation (2.21).

In order to compare the importance of each term in the extended model M1 the variables are non-dimensionalized by using the following scaling:

$$[\omega, \psi] = [U/L, UL] \qquad (2.25)$$

and

$$[x, y, t] = [L, L, T_E], \qquad (2.26)$$

where L and U are typical horizontal length and velocity scales, respectively. The time is non-dimensionalized by using the Ekman timescale $T_E = 2/(f E^{1/2})$. In non-dimensional form, model M1 (2.22) is then written as

$$\underbrace{\tfrac{1}{2} E^{1/2} \frac{\partial \omega}{\partial t}}_{I} + \underbrace{\epsilon J(\omega, \psi)}_{II} - \underbrace{\tfrac{1}{2} E^{1/2} \epsilon \nabla \psi \cdot \nabla \omega}_{III} = \underbrace{E \delta^2 \nabla^2 \omega}_{IV} - \underbrace{\tfrac{1}{2} E^{1/2} \epsilon \omega^2}_{V} - \underbrace{\tfrac{1}{2} E^{1/2} \omega}_{VI}. \qquad (2.27)$$

Besides the Ekman number, the Rossby number ($\epsilon = U/fL$) and the aspect ratio of the vertical and horizontal scales ($\delta = H/L$) appear.

In the conventional model M2, the $O(E^{1/2}\epsilon)$ terms in (2.27) have been neglected under the assumption of small Rossby number. These neglected terms represent the correction to the advection of relative vorticity (III) and the nonlinear contribution in the stretching effects (V). Note that lateral viscous effects, represented by term IV, are still considered. However, under experimental conditions these terms are usually smaller than, or at most of the same order as, the nonlinear corrections III and V. For typical vortices in the laboratory, $E \approx 10^{-4}$, $\delta \approx 4$, and $\epsilon \approx 0.5$. Thus, $E\delta^2 \approx 1.6 \times 10^{-3}$, while $E^{1/2}\epsilon \approx 5 \times 10^{-3}$. Therefore, it is concluded that terms III and V should also be included, in order to improve the two-dimensional model.

3. Testing the model

The extended model M1, given by (2.19), (2.20), (2.21) and (2.22), is tested by means of laboratory experiments and numerical simulations. The laboratory experiments concerned the spin-down of non-isolated cyclonic vortices in a rotating tank. In addition, experimental results of vH91 were also used for studying the evolution of isolated vortices. Non-isolated vortices have a non-vanishing circulation, i.e. they contain a non-zero net amount of vorticity, while isolated vortices have zero net vorticity. Vortices of the latter type may become unstable and transform into tripolar structures (vH91; Kloosterziel & van Heijst 1991). The numerical simulations consisted of solving (2.21) and (2.22) by means of a finite differences code, and the results are compared with the experimental data.

Thus model M1 is tested in two parts: (1) Experiments on the decay of non-isolated vortices are performed; typical vortex parameters (radius of maximum velocity, peak vorticity in the core, etc.) are measured during more than one Ekman period (which is the decay time scale due to bottom friction), and compared with numerical solutions using model M1. (2) The evolution and decay of isolated vortices are simulated numerically, and the results are compared with the experimental data of vH91. In both cases, model M1 is also compared with numerical simulations using model M2.

Before showing the results obtained, the experimental arrangement and the numerical code are briefly discussed in the following two subsections.

3.1. *Experimental arrangement*

The laboratory experiments were performed in a rotating tank filled with fresh tap water. The horizontal size of the rectangular tank is $1\,\mathrm{m} \times 1.5\,\mathrm{m}$. The tank rotates in the anticlockwise direction at a constant rate $\Omega = 0.5\,\mathrm{s}^{-1}$, which corresponds to a Coriolis parameter $f = 2\Omega = 1\,\mathrm{s}^{-1}$.

The flow was visualized by tracer particles floating on the surface, and its evolution could be recorded by a co-rotating camera mounted some distance above the rotating tank. The tracer particles were sprinkled all over the free surface, so that information was obtained about the flow in the entire tank. The video images obtained were processed with the digital image processing package DigImage (Dalziel 1992). With this technique, the positions and velocities of large numbers of tracers can be determined. Subsequently, the velocity data are interpolated onto a rectangular grid in order to facilitate calculation of the vorticity and stream function fields.

In this paper, two types of cyclonic vortices in the rotating tank fluid are studied, namely the so-called 'sink' and 'stirring' vortices. The sink vortices have a single-signed vorticity and are hence non-isolated, while stirring vortices consist of a core surrounded by an annulus of oppositely-signed vorticity in such a way that vortices are isolated. In this study, only experiments on non-isolated vortices are performed, while the experimental results on isolated vortices are taken from vH91. Sink vortices can be produced by locally syphoning a fixed amount of fluid, during a certain period of time, through a thin perforated tube. Stirring vortices are created by placing a small, bottomless cylinder in the tank, stirring the fluid in the cylinder, and then removing it, thus releasing the vortex in the ambient solidly-rotating fluid (for further details on both methods see e.g. vH91 and KvH92).

For the flat-bottom case, typical radial distributions of the vorticity and azimuthal velocity are, for non-isolated vortices,

$$\omega_{sink}(r) = \omega_0 \exp\left(\frac{-r^2}{R^2}\right), \tag{3.1}$$

$$v_{sink}(r) = \frac{R^2 \omega_0}{2r} \left[1 - \exp\left(\frac{-r^2}{R^2}\right) \right], \qquad (3.2)$$

while for isolated vortices

$$\omega_{stir}(r) = \omega_0 \left(1 - \frac{r^2}{R^2} \right) \exp\left(\frac{-r^2}{R^2}\right), \qquad (3.3)$$

$$v_{stir}(r) = \frac{\omega_0 r}{2} \exp\left(\frac{-r^2}{R^2}\right), \qquad (3.4)$$

where ω_0 is the peak vorticity, R a horizontal length scale, and r the radial distance to the centre of the vortex. Typical vortex parameters for the laboratory experiments discussed here are $\omega_0 \approx 3$ to $5\,\mathrm{s}^{-1}$ and $R \approx 2$ to $4\,\mathrm{cm}$.

3.2. *Numerical simulations*

The laboratory experiments are numerically simulated by solving (2.21) and (2.22) with a finite differences code. This code was originally developed by Orlandi and Verzicco (see e.g. Orlandi 1990) for purely two-dimensional flows, and later extended by van Geffen (1998) in order to include rotational effects. Later, topographic variations were included in the code in order to study the effect of bottom topography on barotropic vortices (Zavala Sansón & van Heijst 2000; Zavala Sansón, van Heijst & Doorschot 1999). In this paper, the effect of Ekman friction on flow over a flat bottom is included.

In the simulations, the experimental domain was discretized by 128×128 grid points, which has proven to give a reasonably good resolution for the present rotating tank experiments (see e.g. Zavala Sansón & van Heijst 1999) and to be computationally inexpensive. Additional simulations with doubled grid resolution showed very similar results in all cases.

3.3. *Non-isolated vortices*

The first test for the model concerns the decay of a sink vortex over a flat bottom. This problem has been studied before, analytically and experimentally, by a number of authors (see e.g. KvH92). For this purpose, sink vortices are produced in the rotating tank using three different depths H (24, 18 and 12 cm). The axisymmetric vorticity and velocity distributions of this type of vortex are well approximated by the expressions (3.1) and (3.2). The basic quantities measured in the experiments are the radius of maximum velocity (R_{max}), the maximum velocity (V_{max}), the vortex strength (Γ) and the peak vorticity in the vortex core (ω_0). The method for measuring these parameters consists of fitting the experimental velocities of passive tracers floating at the surface to expression (3.2), in order to obtain R and ω_0, and then obtaining $\Gamma = \omega_0 \pi R^2$. The parameters R_{max} and V_{max} are directly measured. Afterwards, these values are compared with the corresponding numerical simulations. Obviously, the vortex peak vorticity, strength and maximum velocity decrease in time. With regard to the radius of maximum velocity, it is expected that a gradual increase will be observed, due to the Ekman condition at the bottom (see e.g. KvH92; M93; García Sánchez & Ochoa 1995). Indeed, the relative vorticity is positive in the vortex core and therefore the vertical velocity induced by the Ekman layer is also positive (upwards), hence giving rise to an expansion of the vortex. The experiments had a duration longer than the corresponding Ekman period T_E. Table 1 shows the initial vortex parameters (60 s after the forcing was stopped) and the corresponding Ekman periods.

Experiment	H (cm)	T_E (s)	ω_0 (s^{-1})	R (cm)
1	24	339	2.88	3.14
2	18	255	3.26	2.86
3	12	170	3.10	3.07

TABLE 1. Characteristic parameter values for the experiments on the decaying sink vortex over a flat bottom. The calculation of the Ekman periods is based on $f = 1\,\text{s}^{-1}$ and $\nu = 0.01\,\text{cm}^2\,\text{s}^{-1}$ (the kinematic viscosity of water at 20°C).
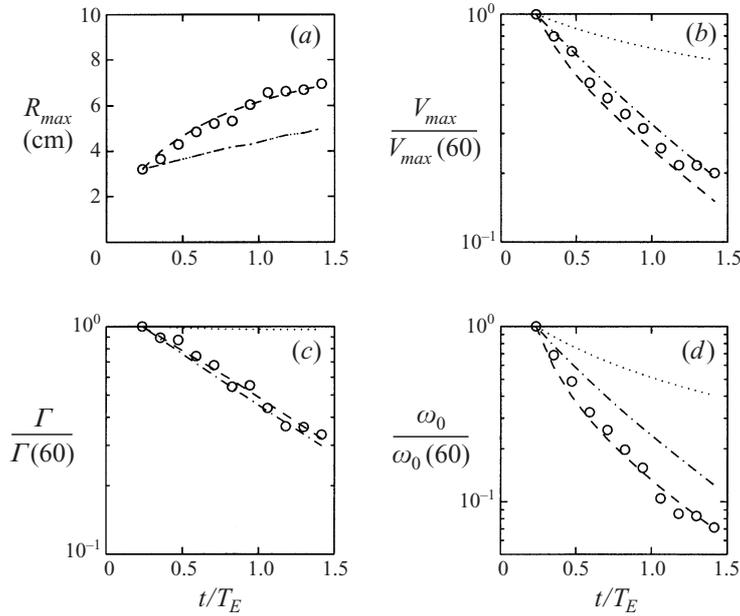
FIGURE 2. Time evolution of the sink vortex parameters in experiment 2 ($H = 18$ cm): (*a*) radius of maximum velocity (R_{max}), (*b*) maximum velocity (V_{max}), (*c*) vortex strength (Γ), and (*d*) peak vorticity (ω_0). Circles denote experimental measurements. The dashed line (— — —) represents the numerical simulation using M1 (extended model), the dashed-dotted line (— · — · —·) M2 (linear Ekman damping) and the dotted line (· · ·) M3 (without Ekman effects). (60) denotes initial parameters 60 s after the forcing was stopped.

For the moment, attention is focused on experiment 2. Figure 2 shows the evolution of the vortex parameters (R_{max}, V_{max}, Γ and ω_0) measured in the experiment (circles) and the corresponding numerical simulations. The dashed line is calculated numerically by solving model M1, while the dashed-dotted line represents the result obtained by solving M2. The dotted line shows the conventional two-dimensional model M3, i.e. without any bottom friction term, but including lateral viscous effects. The time evolution is non-dimensionalized by using the corresponding Ekman time T_E. The plots are made such that they can be easily compared with figures 5 and 9 of KvH92. These authors show the R_{max} and V_{max} evolution of 'collapse' vortices but also one case of a sink vortex.

First, it is evident that the results obtained with model M1 (dashed line) fit the experimental results much better than any of the other curves. From the M3 result in figure 2(*a*), note that there is an increment in R_{max} due only to lateral viscous effects
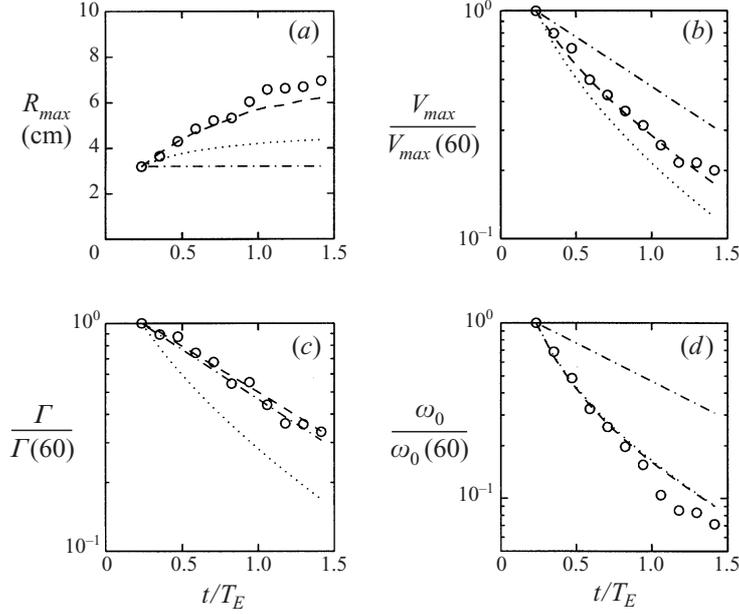
FIGURE 3. Same experimental data (circles) as in figure 2, compared with numerical simulations without including lateral viscous effects. The dashed line $(-\,-\,-)$ represents the M1 simulation, the dashed-dotted line $(-\cdot-\cdot-\cdot)$ M2, and the dotted line $(\cdot\cdot\cdot)$ is obtained by using M1 without lateral viscous effects and advective terms.

(see Kloosterziel 1990*a*). It is clear that M2 does not give any additional contribution to this R_{max} expansion, since it coincides with M3; however, both of them fail to predict the correct R_{max} evolution, in contrast to M1. This is not surprising, since the linear Ekman term only contributes to the vortex decay, without any radial advection of V_{max}. Note also that M2 underestimates the decay of the maximum velocity V_{max} (see figure 2*b*) and the peak vorticity ω_0 (see figure 2*d*). The additional damping and the R_{max} increase in M1 is due to the nonlinear Ekman terms, as will be discussed below and in the discussion section. Also note that the vortex strength (figure 2*c*) is well predicted by M2.

In order to show the role of the Ekman terms in M1 more clearly, figure 3 presents the same experimental results, but now compared with numerical simulations in which the lateral viscous effects, term IV of (2.27), are omitted. Note that the Jacobian term II is very small in this quasi-axisymmetric example. As before, the dashed-line corresponds to M1 and the dashed-dotted line to M2. The dotted line now corresponds to the reduced model M1, in which the Ekman advective effects (term III) are also omitted; this latter simulation was performed in order to appreciate the effect of this term.

The main results are the following. First, note that M1 gives a reasonable approximation to the experimental data even without lateral viscous effects, which clearly indicates the smallness of these terms. Second, when omitting lateral viscous effects and the Jacobian term, M2 has the solution (Greenspan & Howard 1963)

$$\omega = \omega_0 \exp\left(-t/T_E\right). \tag{3.5}$$

Because there are no lateral viscous effects, R_{max} remains constant, and the other parameters decay exponentially as $\exp\left(-t/T_E\right)$. Third, the simulation without lateral
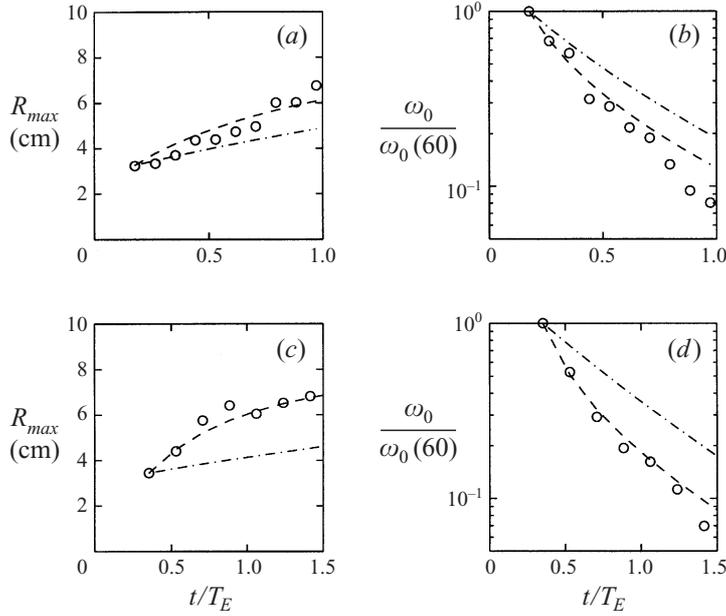
FIGURE 4. Time evolution of the sink vortex parameters in experiments 1 ($H = 24$ cm) and 3 ($H = 12$ cm): (*a*) and (*c*) radius of maximum velocity (R_{max}), (*b*) and (*d*) peak vorticity (ω_0). Circles denote experimental measurements. The dashed line ($-\,-\,-$) represents the numerical simulation using M1 (extended model) and the dashed-dotted line ($-\cdot-\cdot-$) M2 (linear Ekman damping).

viscosity and advective terms (reduced model M1, dotted line) has the solution (Kloosterziel 1990*b*)

$$\omega = \frac{\omega_0 \exp(-t/T_E)}{(\omega_0/f)[1 - \exp(-t/T_E)] + 1} \tag{3.6}$$

for the peak vorticity decay, figure 3(*d*). However, the R_{max} increase is slower than in M1, and therefore, the vortex strength decays faster. This simulation clearly shows the role of the advective Ekman terms: they provide a larger vortex expansion, while the peak vorticity decay is only slightly affected. Recall that this observation is made for these simulations in which lateral viscous effects are neglected.

Finally, the results for experiments 1 ($H = 24$ cm) and 3 ($H = 12$ cm) show a similar behaviour to experiment 2 (see figure 4). In these cases, model M1 also provides a better prediction for the evolution of the vortex parameters than models M2 and M3. From previous examples, it may be concluded that M1 simulates the laboratory experiments on a decaying non-isolated vortex over a flat bottom very well.

3.4. *Isolated vortices: the tripole formation*

Isolated cyclonic vortices in rotating tank experiments are often observed to evolve towards a tripolar structure, formed by a cyclonic core with two anticyclonic satellites. This type of vortex was experimentally studied by vH91 and numerically by OvH92, where model M2 was used. Therefore, in order to test the new model M1, the results in these two papers are compared with numerical simulations using the extended model.

All the parameters in the present numerical simulations are chosen the same as those in OvH92, except the mean depth, which was $H = 15$ cm in their case, while here $H = 18$ cm, corresponding to the experimental value in vH91. The rest of
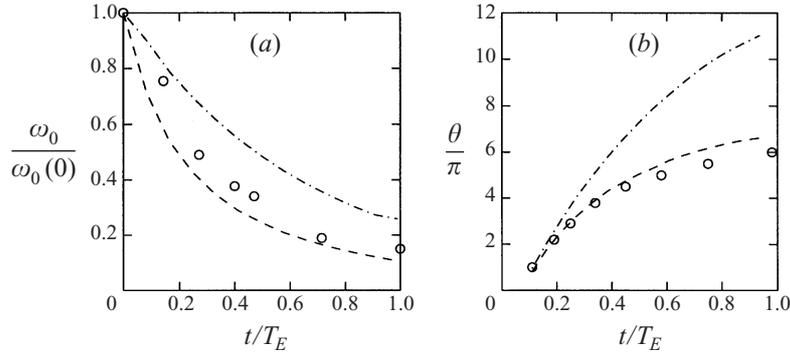
FIGURE 5. Time evolution of (a) the stirring vortex peak vorticity (tripole core) and (b) the tripole orientation angle. In both plots, dashed lines (− − −) denote the numerical simulations using M1, and the dashed-dotted lines (− · − · −·) represent the M2 simulations.

the flow parameters are the reference velocity $U = 26.4\,\mathrm{cm\,s^{-1}}$, the characteristic length scale $L = 4\,\mathrm{cm}$, the kinematic viscosity $v = 0.01\,\mathrm{cm^2\,s^{-1}}$, and the Coriolis parameter $f = 2\,\mathrm{s^{-1}}$. The vortex parameters in equations (3.3) and (3.4) are given by $\omega_0 = U/L$ and $R = \sqrt{2}L$. The domain was a square box of $30\,\mathrm{cm} \times 30\,\mathrm{cm}$ with free-slip walls, discretized with a 128×128 rectangular grid. Also, the initial vorticity distribution given by (3.3) was randomly perturbed using a similar method to OvH92. A perturbation of this type leads to the formation of a tripolar vortex structure.

There are three methods of comparing the present results with those in vH91 and OvH92: measuring the peak vorticity decay in the vortex core; measuring the anticlockwise rotation of the whole tripole structure; making scatter plots, which show the ω–ψ relationship during the tripole evolution. In all cases, model M1 proves to give better results than M2.

Figure 5(a) shows the experimental results of vH91 for the peak vorticity decay at the core of the tripole (circles). The dashed and dashed-dotted lines represent the numerically calculated peak vorticity values, $\omega_0(t)$, using M1 and M2, respectively. The time has been non-dimensionalized with the Ekman time scale $T_E = 180\,\mathrm{s}$. This plot shows that M1 gives a better prediction for the peak vorticity decay. This result is not conclusive, however, since the M2 prediction is not too far off the observational data. Indeed, this is similar to what was observed in the non-isolated vortex case, figure 2(d), where the prediction for the peak vorticity decay was somewhat better in M1 than in M2, although the difference was not really large.

A much stronger test for the new model is presented in figure 5(b), which shows the anticlockwise tripole orientation angle (θ) as a function of time. In the laboratory experiment, θ was measured during an Ekman period, in which the tripole performed three revolutions. The good agreement between the experimental results and the M1 prediction is remarkable. The discrepancy between the model calculations and the laboratory observations is less than one fourth of a revolution. In contrast, the M2 prediction fails by more than two and a half revolutions. (Note that there is an error in the experimental values shown in OvH92, figure 6, which is attributed to the typographical error in the vertical scale of figure 9, in vH91.)

An additional test for M1 is obtained by means of scatter plots. Such plots are useful to diagnose stationary two-dimensional structures in inviscid flows (governed by $\partial\omega/\partial t + J(\omega, \psi) = 0$), since a well-defined ω–ψ relationship in such plots (i.e. $\omega = F(\psi)$) indicates that the Jacobian term is zero. Obviously, the tripolar vortex is

not a stationary structure, due to its anticlockwise rotation. However, vH91 produced scatter plots in a reference frame co-moving with the tripole, seeking the possible stationarity of the flow in such a coordinate system. In this particular frame, the corrected ω and ψ values are given by

$$\psi^* = \psi + \tfrac{1}{2}\dot{\theta}r^2 \tag{3.7}$$

and

$$\omega^* = \omega - 2\dot{\theta}. \tag{3.8}$$

Figures 6(a) and 6(b), show the calculated ω^*–ψ^* relationship for three different times, using M2 and M1, respectively. These plots can be compared with the corresponding experimental results in vH91 (their figures 15a, c and d) shown in figure 6(c). As explained in that paper, tripole scatter plots are formed by three main branches: the positive vorticity core, the negative vorticity in the satellites and the negative constant vorticity in the ambient fluid, outside the tripole. It is very clear that the numerical results obtained with the new model are much more satisfactory than those obtained with the conventional model. Note that the substantial dispersion shown in the experiments is also present in M1, and not in M2. In particular, the negative peak values in the satellites, which decay slower than the vortex core, are well simulated in M1, even for later stages ($t = 120$ s). As mentioned in vH91, this is due to the difference in decay time scales between positive and negative vortices, which is larger in the negative satellites; this effect is captured by including the nonlinear Ekman terms in the new model. Similar plots are also given in OvH92; however, direct comparison has not been made because their numerical simulation used $H = 15$ cm, instead of 18 cm, which gives a different value for $\dot{\theta}$ in the ω^*–ψ^* corrections.

4. Summary and discussion

A two-dimensional model including damping effects associated with the no-slip condition at a flat bottom has been derived (model M1). This model incorporates the frictional effects due to the solid bottom by means of the linear Ekman theory, which predicts the vertical velocity induced by the thin Ekman layer at the bottom. In this model, nonlinear Ekman terms in the vorticity equation are also included, and a suitable ω–ψ formulation is found, see (2.22) or (2.27). These terms are usually neglected in conventional two-dimensional models since they are considered small due to the low Rossby number assumption, a prerequisite for using the linear Ekman theory. The most common two-dimensional model including Ekman damping effects, model M2, only contains a linear term in the vorticity equation, see (2.23). Usually, model M2 and the purely two-dimensional model M3 (i.e. without Ekman friction, see (2.24)) also include lateral viscous effects. For the experimental cases considered here, however, these terms are actually as small as the nonlinear Ekman terms (see §2). Therefore, it is proposed that a more complete two-dimensional model should include these nonlinear effects, even though the Rossby number of the flow is small. In fact, it has been suggested before (e.g. KvH92; M93) that linear Ekman theory still applies for moderate Rossby numbers, which reinforces the idea of including those nonlinear Ekman terms. One additional advantage of model M1 is that viscous effects can be separated and studied independently. These effects are the Ekman advection effects (term III in (2.27)), the lateral viscosity (IV), and the nonlinear (V) and linear (VI) Ekman stretching effects on fluid columns. Also, horizontal velocities in model M1 have a small correction due to Ekman effects, proportional to $E^{1/2}$.
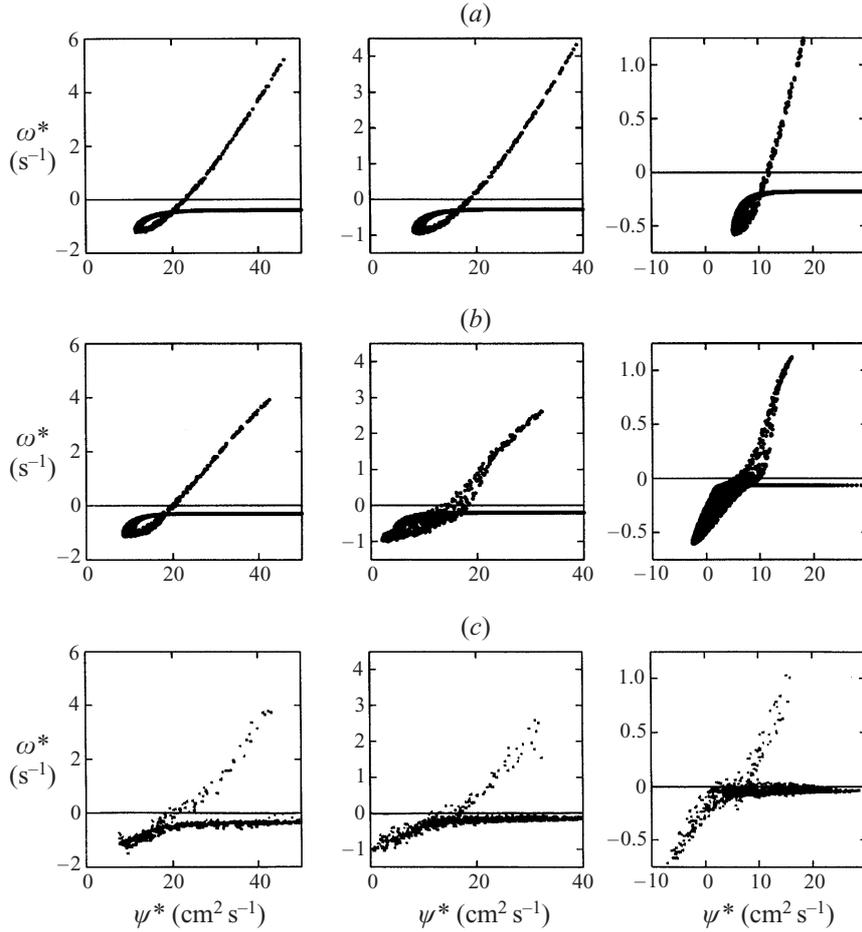
FIGURE 6. Numerically calculated scatter plots showing the corrected ω^*–ψ^* relation representing the tripole evolution at three different times ($t/T_E = 0.11$, 0.25 and 0.67). (*a*) Model M2, (*b*) model M1 and (*c*) experimental plots (taken from vH91).

The extended two-dimensional model M1 has been applied to study the decay of experimental barotropic vortices. These vortices are cyclonic structures, either non-isolated (mostly with single-signed vorticity) or isolated (a vortex core surrounded by oppositely-signed vorticity). In the laboratory, non-isolated vortices are usually met in the form of stable cyclones (KvH92), which remain approximately axisymmetric, while decaying by Ekman damping and lateral viscous effects. These vortices are characterized by their radius of maximum velocity (R_{max}), the maximum velocity (V_{max}), the vortex strength (Γ) and the peak vorticity in the vortex core (ω_0). Measurements of these quantities in laboratory experiments have been compared with numerically calculated values of simulations based on the extended model M1 and the conventional models M2 and M3. The results show that model M1 gives a better representation of the vortex evolution than conventional models, which do not include the nonlinear Ekman terms. It is found that the well-known vortex expansion (increase of R_{max}) is not only due to lateral viscosity (Kloosterziel 1990a) and to nonlinear stretching effects (KvH92; M93) but also to nonlinear advection effects, driven by the Ekman layer. This was shown by comparing numerical results from calculations with and without
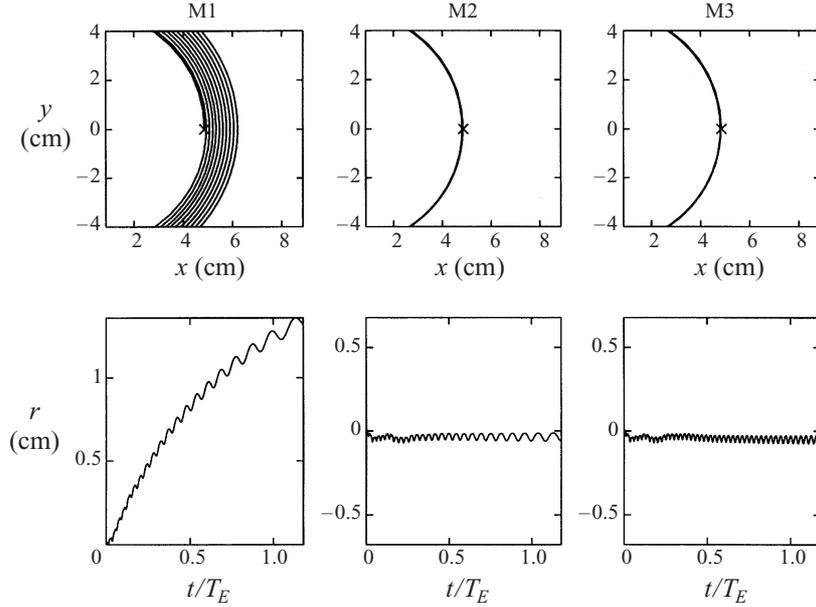
FIGURE 7. Upper row: calculated trajectories of a passive tracer in a non-isolated vortex, using models M1, M2 and M3 (as in figure 2). The initial position of the tracer ($\times$) is $(x_0, y_0) = (1.7R, 0)$. Lower row: time evolution of the radial distance of the tracer from the circle of radius $1.7R$. The small oscillations are attributed to the grid discretization.

including lateral viscous effects, stretching Ekman effects and advective Ekman terms. In addition to the R_{max} expansion, the Ekman advection effects in M1 lead to a remarkable difference with respect to M2 and M3. In these models, there is no outward advection of fluid, since the Jacobian term vanishes for axisymmetric flows. This implies that the material trajectories are circles. In contrast, the Ekman advective effects induce material particles to move outward in a spiral fashion. This is shown in figure 7, where the calculated trajectories of a passive tracer are plotted. The initial position of the tracer is $(x_0, y_0) = (1.7R, 0)$. The trajectories are obtained from the simulations shown in figure 2, i.e. using M1, M2 and M3. Figure 7 also shows the radial distance of the particle from the circle of radius $1.7R$ as a function of time; the tracer moves outward in model M1, but remains at a fixed radius in models M2 and M3.

Some previous studies have also taken into account the nonlinear Ekman corrections in the special case of axisymmetric flows. For instance, a basic model for spin-up in a rotating cylinder was developed by Wedemeyer (1964). This model was later extended by a number of authors (e.g. KvH92 and M93) in order to study the spin-down of barotropic vortices. The Wedemeyer model considers the azimuthal component of the Navier–Stokes equation, written in cylindrical coordinates (r, θ), while assuming axisymmetric flow ($\partial/\partial\theta = 0$); in dimensional form

$$\frac{\partial v_\theta}{\partial t} + u_r(\omega + f) = v \frac{\partial \omega}{\partial r}, \tag{4.1}$$

where u_r and v_θ are the radial and azimuthal velocity components, respectively, and the relative vorticity ω is defined as

$$\omega = \frac{1}{r} \frac{\partial}{\partial r}(r v_\theta). \tag{4.2}$$

When the bottom Ekman condition is considered, it is found that u_r is proportional to $E^{1/2}v_\theta/2$ (in non-dimensional terms, KvH92 found $u_r = v_\theta/2$). This result, together with (4.1) and (4.2), is used to derive the vorticity equation:

$$\frac{\partial \omega}{\partial t} + \tfrac{1}{2}E^{1/2}v_\theta\frac{\partial \omega}{\partial r} + \tfrac{1}{2}E^{1/2}\omega(\omega + f) = \nu\frac{1}{r}\frac{\partial}{\partial r}\left(r\frac{\partial \omega}{\partial r}\right). \tag{4.3}$$

For comparing with the extended model M1, take into account that the Jacobian term *II* in (2.27) vanishes for axisymmetric flows. In this case, after a change of coordinates, it is found that term *III* becomes the advective term in (4.3) (with $v_\theta = \partial\psi/\partial r$), and term *IV* in (2.27) corresponds with the right-hand side of (4.3). In other words, for the axisymmetric case, (2.22) reduces to (4.3). The obvious advantage of model M1 is that is not restricted to axisymmetric flows, and therefore it can be used to study non-axisymmetric cases (see below).

On the other hand, isolated vortices may be unstable (Kloosterziel & van Heijst 1991) and lead to the formation of tripolar structures, which consist of a cyclonic core and two anticyclonic satellites. Such a structure rotates as a whole in an anticlockwise sense, while gradually slowing down. The experimental data of vH91, where laboratory tripolar vortices were studied, have been compared with the corresponding numerical simulations using model M1. Three measurements confirmed the better performance of M1 in comparison with M2. This applies to (*a*) the decay of the core vorticity, (*b*) the tripole orientation angle, and (*c*) the scatter plots, showing the relation between the corrected values of the relative vorticity ω^* and the stream function ψ^* in a frame co-rotating with the tripole. In particular, the error in the tripole's azimuthal orientation θ using M1 was less than one fourth of a revolution after a time-span of one Ekman period T_E. In contrast, model M2 showed a discrepancy of more than two and a half revolutions. Also, the scatter plots confirmed the slower decay of the negative-vorticity satellites compared with the positive-vorticity core, which was suggested in other studies (vH91; OvH92). Kloosterziel (1990*b*) pointed out this difference between cyclones and anticyclones by applying (3.6) to the peak vorticity in the core of a tripolar vortex. From this expression, it is evident that $\omega_0 < 0$ implies a slower peak vorticity decay than $\omega_0 > 0$.

It must be remarked that, as in model M2, the linear Ekman condition (2.9) is used as the lower boundary condition. Without this assumption, the pumping from the Ekman layer should be proportional to $\omega + O(\epsilon)$ instead of just ω. This correction, due to ageostrophic effects, would yield an additional term $O(E^{1/2}\epsilon)$ in the stretching terms $E^{1/2}[\omega + O(\epsilon)](\omega + f)$. In the present approximation, i.e. using (2.9), the 'extra' vertical velocity is not taken into account. The justification for using the linear Ekman condition is empirical, as shown by the experimental results in this paper. Calculation of the $O(\epsilon)$ correction in the Ekman condition may be a difficult procedure (see e.g. Hart 1995, 2000). The present model, however, is quite simple and the laboratory experiments can be simulated very effectively. Since the main purpose is to understand the essential dynamics involved in the decay process, this study is focused on understanding a simple two-dimensional model such as M1, rather than deriving more complicated formulations, often difficult to interpret. Work is in progress on the extension of model M1 to non-flat bottom topographies and the results will be published elsewhere.

REFERENCES

DALZIEL, S. 1992 *Digimage. Image Processing for Fluid Dynamics*. Cambridge Environmental Research Consultants Ltd., Cambridge, UK.

GARCÍA SÁNCHEZ, R. F. & OCHOA, J. 1995 Decaimiento de vórtices barotrópicos en el plano f. *Rev. Mex. Fís.* **41**, 533–555 (in Spanish).

GEFFEN, J. H. G. M. VAN 1998 *NS-evol*. Internal report R-1466-D, Fluid Dynamics Laboratory, Department of Physics, Eindhoven University of Technology, The Netherlands.

GREENSPAN, H. P. & HOWARD, L. N. 1963 On a time dependent motion of a rotating fluid. *J. Fluid Mech.* **17**, 385–404.

HART, J. E. 1995 Nonlinear Ekman suction and ageostrophic effects in rapidly rotating flows. *Geophys. Astrophys. Fluid Dyn.* **79**, 201–222.

HART, J. E. 2000 A note on nonlinear corrections to the Ekman layer pumping velocity. *Phys. Fluids* **12**, 131–1135.

HEIJST, G. J. F. VAN., KLOOSTERZIEL, R. C. & WILLIAMS, C. W. M. 1991 Laboratory experiments on the tripolar vortex in a rotating fluid. *J. Fluid Mech.* **225**, 301–331 (referred to herein as vH91).

KLOOSTERZIEL, R. C. 1990*a* On the large-time asymptotics of the diffusion equation on infinite domains. *J. Engng Maths* **24**, 213–236.

KLOOSTERZIEL, R. C. 1990*b* Barotropic vortices in a rotating fluid. PhD thesis, Eindhoven University of Technology.

KLOOSTERZIEL, R. C. & HEIJST, G. J. F. VAN 1991 An experimental study of unstable barotropic vortices in a rotating fluid. *J. Fluid Mech.* **223**, 1–24.

KLOOSTERZIEL, R. C. & HEIJST, G. J. F. VAN 1992 The evolution of stable barotropic vortices in a rotating free-surface fluid. *J. Fluid Mech.* **239**, 607–629 (referred to herein as KvH92).

KONIJNENBERG, J. A. VAN DE 1995 Spin-up in non-axisymmetric containers. PhD thesis, Eindhoven University of Technology.

MAAS, L. R. 1993 Nonlinear and free-surface effects on the spin-down of barotropic axisymmetric vortices. *J. Fluid Mech.* **246**, 117–141 (referred to herein as M93).

ORLANDI, P. 1990 Vortex dipole rebound from a wall. *Phys. Fluids* A **2**, 1429–1436.

ORLANDI, P. & HEIJST, G. J. F. VAN 1992 Numerical simulation of tripolar vortices in two-dimensional flow. *Fluid Dyn. Res.* **9**, 179–206 (referred to herein as OvH92).

PEDLOSKY, J. 1987 *Geophysical Fluid Dynamics*. Springer.

WEDEMEYER, E. H. 1964 The unsteady flow within a spinning cylinder. *J. Fluid Mech.* **20**, 383–399.

ZAVALA SANSÓN, L. & HEIJST, G. J. F. VAN 2000 Interaction of barotropic vortices with coastal topography: Laboratory experiments and numerical simulations. *J. Phys. Oceanogr.* (in press).

ZAVALA SANSÓN, L., HEIJST, G. J. F. VAN & DOORSCHOT, J. J. J. 1999 Reflection of barotropic vortices from a step-like topography. *Il Nuovo Cimento C* **22**, 909–929.